Article

Automatic Coastline Extraction Based on the Improved Instantaneous Waterline Extraction Method and Correction Criteria Using SAR Imagery

Hongxia Zheng [1], Xiao Li [2], Jianhua Wan [1,*], Mingming Xu [1], Shanwei Liu [1] and Muhammad Yasir [1]

1   College of Oceanography and Space Informatics, China University of Petroleum, Qingdao 266580, China
2   Qilu Aerospace Information Research Institute, Jinan 250100, China
*   Correspondence: 19850014@upc.edu.com

Abstract: Coastlines with different morphologies form boundaries between the land and ocean, and play a vital role in tourism, integrated coastal zone management, and marine engineering. Therefore, determining how to extract the coastline from satellite images quickly, accurately, and intelligently without manual intervention has become a hot topic. However, the instantaneous waterline extracted directly from the image must be corrected to the coastline using the tide survey station data. This process is challenging due to the scarcity of tide stations. Therefore, an improved instantaneous waterline extraction method was proposed in this paper with an integrated Otsu threshold method, a region-growing algorithm, Canny edge detection, and a morphology operator. Based on SAR feature extraction and screening, the multi-scale segmentation method and KNN classification algorithms were used to achieve object-oriented automatic classification. According to different types of ground features, the correction criteria were presented and used in correcting the instantaneous waterline in biological coasts and undeveloped silty coasts. As a result, the accurate extraction of the coastline was accomplished in the area of the Yellow River Delta. The coastline was compared with that extracted from the GF-1 optical image. The result shows that the deviation degree was less than the field distance represented by three pixels.

Keywords: SAR image; instantaneous waterline; coastline extraction; KNN method; correction criteria

1. Introduction

The coastline represents the primary data for the integrated management of the coastal zone [1,2]. Rapid and accurate coastline extraction is of great significance to coastal zone resource planning and management, environmental protection, and navigation safety [3,4]. The coastline can be obtained through field surveys. Although the data are very accurate, gathering the data is expensive, inefficient, and time-consuming [5]. Remote sensing technology has the advantage of covering an extensive observation range, facilitating periodic observation, and providing data promptly with good economic benefits [6]. Coastline extraction from remote sensing images is a commonly used method [7–9]. Visual interpretation and automatic interpretation are two commonly used methods for coastline extraction. Among them, visual interpretation requires the interpreter to have extensive experience and is inefficient. Hence, automatic interpretation has become a hot research topic for scholars [10–19] because they provide data rapidly and with strong reusability [5,6].

In addition, compared with optical images, high-resolution polarimetric SAR images provide systematic acquisitions characterized by all-day and almost-all-weather meter-level spatial resolution [20], providing high-quality and reliable data support for automatic coastline extraction [21].

Polarimetric SAR imagery includes an unprecedented amount of information regarding the scattering scene that can be successfully used through, e.g., target decomposition methods, to improve coastline extraction concerning single-polarization SAR im-

agery [22]. These features have been used to extract the instantaneous water boundary [23]. Paes et al. [24] used mixed polarization architecture to realize the classification of coastal features and extracted the coastline from RadarSAT-2 data. Nunziata et al. [25] proposed a new metric based on the correlation between co-polarized and cross-polarized channels for polarized SAR images of C and X bands to extract coastlines from dual-polarized coherent and non-coherent images. Ferrentino et al. [26] proposed a polarization SAR coastline extraction and coastal feature classification method based on Freeman polarization decomposition features. The results showed that it had the best accuracy in detecting a sandy shoreline. The polarimetric SAR images were mapped to the polarization entropy image domain for coastline extraction by analyzing the scattering characteristics of ground objects near the coastline [27,28].

However, the edge of seawater and land on SAR images is the instantaneous waterline at the imaging time, which can be detected [29]. And the instantaneous waterline must be corrected to the specific coastline type to obtain an actual coastline using tide survey station data [30]. This process is challenging because of the scarcity of tide stations. In addition, it is also expensive in terms of computer time.

In light of the current problems associated with coastline extraction, this paper has presented a novel unsupervised method to extract the instantaneous water edge that includes automatic local correction. The method has been verified on actual RadarSAT-2 high-resolution polarimetric SAR imagery. The improved region-growing algorithm determined the ocean region, and the first division between the ocean and the land was completed. The instantaneous waterline was detected by the edge detection algorithm, which was used to construct the mask file. Then, the masked image was classified by the multi-scale segmentation and KNN classification algorithm. Finally, based on the characteristics of the coastline types, this study established the corresponding correction criteria to adjust the extracted instantaneous waterline to the position of the actual coastline and analyzed the precision of the result.

2. Materials and Methods

2.1. Study Area and Data Sources

The Yellow River Delta, with its rich natural resources, was selected as the study area. This area is a critical wetland nature reserve and the largest estuarine delta in China. The delta is located on the south coast of Bohai Bay and the west coast of Laizhou Bay, with coordinates in the range of 117°31′~119°18′ E, 36°55′~38°16′ N, at 10 m and 15 m in altitude above sea level, and covering an area of 5450 km². The estuarine region was our focus area, as it is mainly composed of artificial coastline, undeveloped silty muddy coastline, and biological coastline. Human and natural activities strongly influence the site, and there are frequent and dramatic changes in the coastline. Therefore, coastline extraction is of great value.

This study employed the RadarSAT-2 high-resolution full-polarization image data of 23 September 2015, acquired by a high-resolution commercial satellite equipped with a C-band radar sensor. Table 1 displays the specific parameters of the data. Figure 1 presents the research area and satellite imagery.

Table 1. Remote Sensing Image Data.

| Sensor	Mission Type	Acquisition Date	Image Information	Polarization
Radarsat-2	Radar imaging	2015/9/23 11:31	C-band/SLC /Imaging beam Q5 /Range resolution 12 m /Azimuth resolution 8 m	Full polarization HH/HV/VH/VV
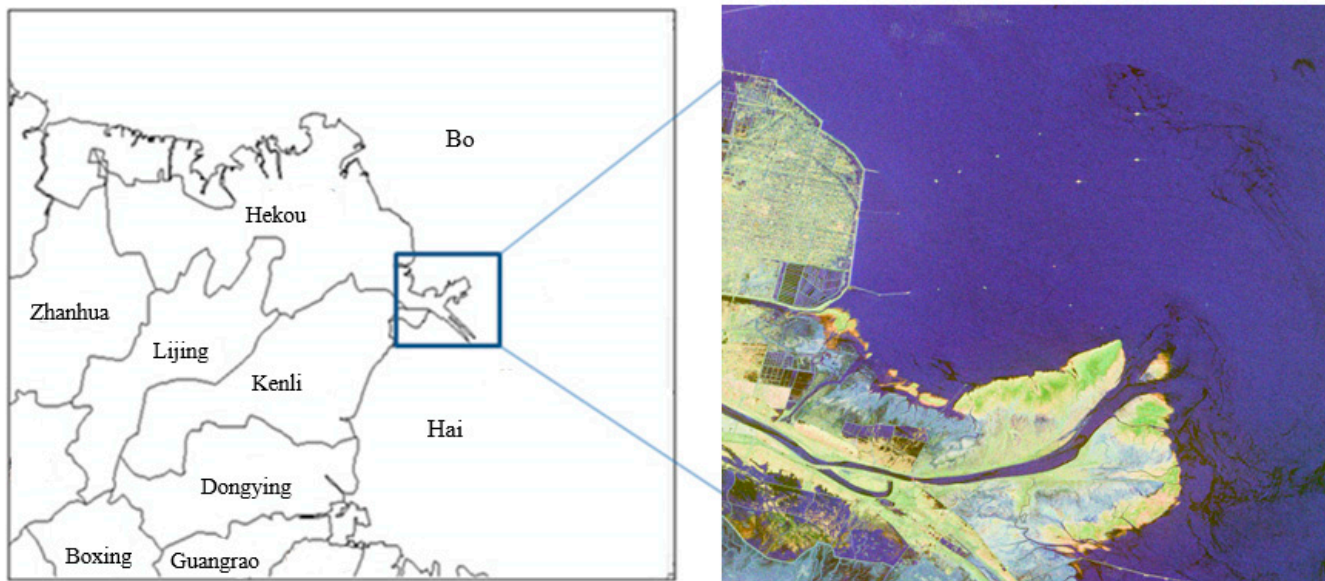
Figure 1. The geographical location of study area.

2.2. Proposed Methods

This study extracted the instantaneous waterline from the SAR image and corrected it using established correction criteria, and the accurate coastline was obtained. First, the collected high-resolution SAR remote sensing image was pre-processed. Then, an improved region-growing algorithm was proposed to extract the instantaneous waterline from the pre-processed images, and the extraction results were used to mask the seawater. Third, automatic classification was accomplished using multi-scale segmentation and the KNN classification algorithm with extracted features. Fourth, a coastline correction criterion was established, and the instantaneous waterline was corrected to the position of the accurate coastline by the classification results. Finally, the accuracy of the extraction result was evaluated with the result of the GF-1 optical image. The technical process is shown in Figure 2.
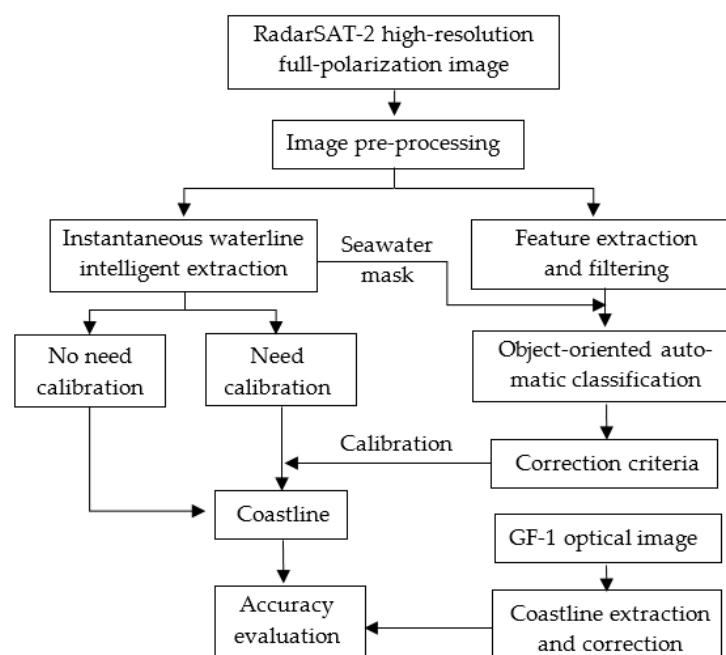
Figure 2. The overall methodology flowchart.

2.2.1. Coastline Definition and Interpretation Characteristics

Coastlines with different morphologies form boundaries between the land and ocean [5]. There are three definitions used in different disciplines, as depicted in Figure 3 [31,32].
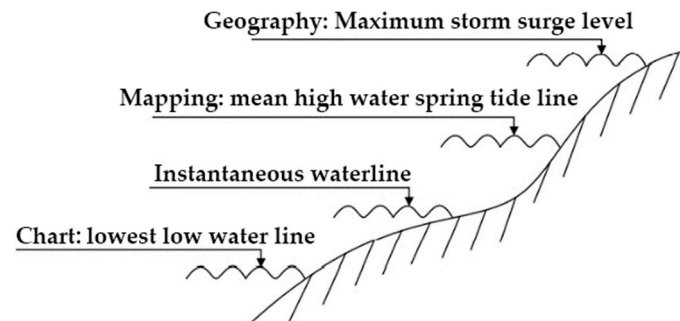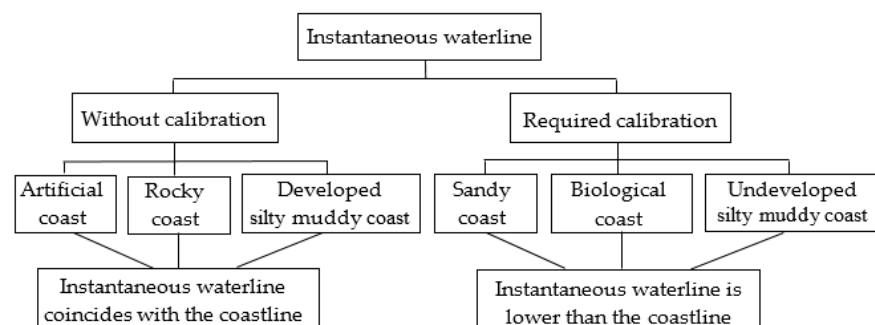

Figure 3. Three types of coastline definition.

- Geography: the location of the maximum storm surge;
- Mapping and marine management: multiannual mean high-water spring tide line;
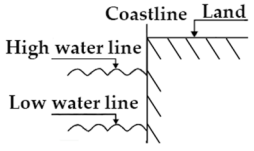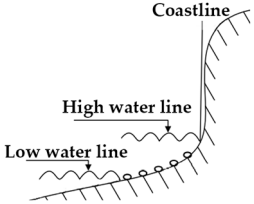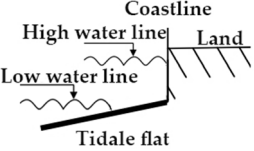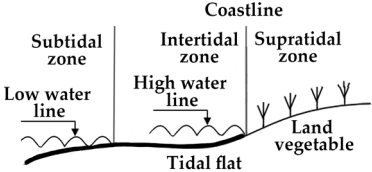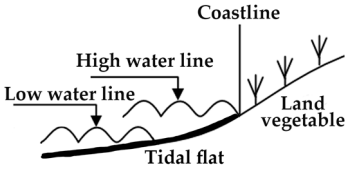- Nautical chart: lowest low-water line.

From Figure 3, it can be seen that the location of the maximum storm surge is the highest, followed by the multiannual mean high-water spring tide line and the lowest low-water line. The boundary line between the seawater and land, known as the instantaneous waterline, is located above the lowest low-water line and below the multiannual mean high-water spring tide line. Affected by tides, the location of the instantaneous water line changes over time, making it non-unique. In this paper, the coastline refers to the multiannual mean high-water spring tide line, whose location does not change over a short period of time. The boundary line extracted from the satellite image was the instantaneous waterline, which differs from the coastline. The coastline can be categorized into five types: artificial coastline, biological coastline, silty muddy coastline, rocky coastline, and sandy coastline. The definition and interpretation characteristics are summarized in Table 2 from an extensive literature review [31–33].

Table 2 shows that the artificial coast and developed silty muddy coast have no slope, and the rocky coast has a steep and short slope. However, the SAR data used in this study was limited by resolution, with a range resolution of 12 m and azimuth resolution of 8 m. The instantaneous waterline extracted from the SAR image of the above three coastline categories did not require correction and coincided with the coastline. The sandy coast, biological coast, and undeveloped muddy coast all have a gradual tidal flat or beach with a long extension distance. The acquisition date of the SAR image was 23 September 2015, when no spring tides occurred in the Yellow River Delta. Therefore, the position of the instantaneous waterline extracted from the SAR image was lower than the coastline, and it must be corrected towards the land direction based on the interpretation characteristics. The above content is shown in Figure 4.

Figure 4. Types of instantaneous waterline.

Table 2. Coastline type and interpretation characteristics.

Coastline Type	Definition	Interpretation Characteristics	Schematic Diagram
Artificial Coast	The artificial coastline is located on the artificial coast, including man-made coastal structures such as border dikes, wharves, breakwaters, revetments, and slopes.	The coastline coincides with the permanent structure, and the boundary line near the land is used as the coastline in sea-closure engineering.	
Rocky Coast	The rocky coastline is located above the rocky coast, which is made up of rocky outcrops, often with prominent headlands and bays that run deeper into the land, and it has a twisting coastline.	The land–water interface of headlands and upright steep cliffs serves as the coastline.	
Silty Muddy Coast	Developed: A large number of shrimp ponds, salt fields, and other economic areas have been constructed on the tidal flat, and the dam has been built to prevent the inflow of high seawater.	The breakwater is the location. of the coastline	
	Undeveloped: The low flat coast shaped by tidal action has a gentle beach-face slope, whose width can be several kilometers or even wider. Generally, tidal creeks are developed, and some tidal creeks' upper ends are connected to the river estuary.	The boundary where the growth status of salt-tolerant plants changes significantly is used as the coastline.	
Biological Coast	Biological coastlines are generally divided into mangrove coastlines, coral reef coastlines, and reed coastlines located on the mangrove coast, coral reef coast, and silty muddy coast, respectively.	The mangrove coastline was determined on the inner mangrove boundary; the reed coastline was determined where there was a marked difference between reed abundance and thinning.	
Sandy Coast	Sandy coasts are formed by the accumulation of sand grains by wave action, and the sand disappears in areas where the waves cannot act.	The boundary between the grit and the non-sand features on the land is regarded as the coastline.	
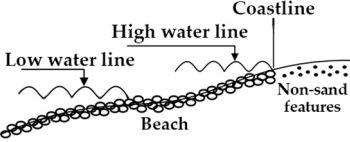
2.2.2. SAR Image Pre-Processing

The Radarsat-2 high-resolution polarized image was pre-processed using PolSARpro software, including coherence matrix T3 extraction, geometry correction, and filter processing. The details are as follows:

(1) **Extraction of the T3 matrix**. The polarization coherence matrix was extracted from the backscattering polarization matrix S, which contained the primary polarization information [34].

(2) **Geometric correction.** Due to the influence of the platform position, atmospheric refraction, terrain, and other factors, the shape, size, and geometric position of objects in remote sensing images are deformed. By employing the bilinear difference method and SRTM data, geocoding and orthographic correction methods were implemented to convert the image coordinates to the WGS84 system. The distortion of the object's shape, size, direction, and geometric position was therefore eliminated [35].

(3) **Filtering processing.** High-resolution polarized SAR images are significantly affected by speckle noise, which affects the later coastline extraction results. The refined Lee filter was applied to filter the SAR image, reducing speckle noise while preserving the polarimetric information [36,37].

2.2.3. Instantaneous Waterline Intelligent Extraction

By integrating the Otsu threshold method [38,39], the region-growing algorithm [40,41], Canny edge detection [42], and the morphology operator [33], an improved and intelligent instantaneous water edge extraction algorithm was proposed. The seed point in the ocean was selected as the starting point of regional growth, and the difference values between the seed point and its neighbors were calculated. Then, the appropriate threshold was found adaptively, and the growth direction of the marine region was determined. Thus, the marine region growth process was completed. The boundary tracking operator was used to detect the land–ocean dividing line, and the instantaneous water boundary was obtained. Figure 5 presents the flowchart of the process.
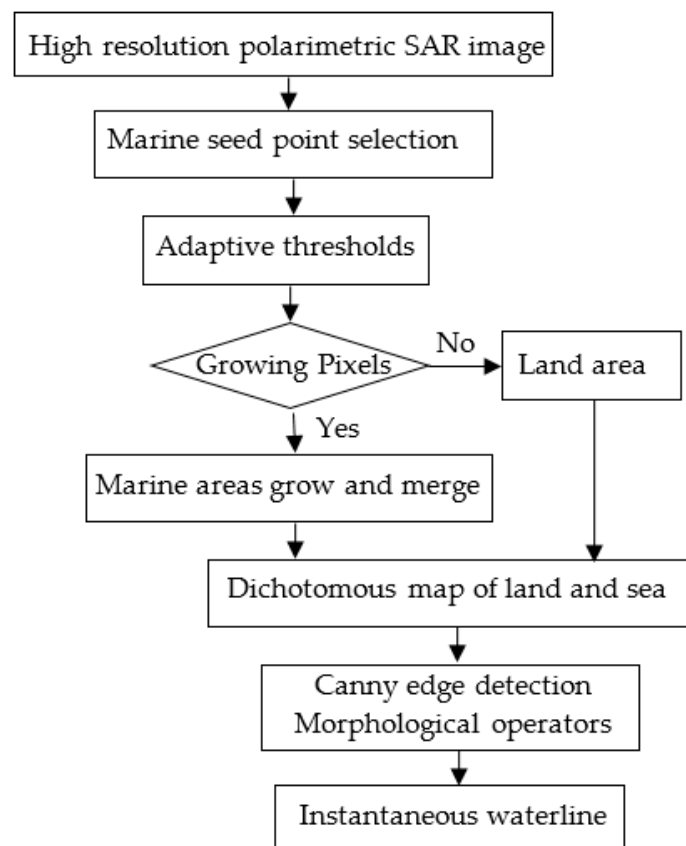
Figure 5. The flowchart of the improved instantaneous waterline extraction algorithm.

(1) **Select the seed node.** A seed pixel was set as the starting point for growth in the ocean region.

(2) **Adopt adaptive thresholds**. The adaptive threshold Otsu was adopted instead of a fixed threshold, in which the image could be divided into the background and target according to the threshold T. If the pixel value of the image was less than the threshold

T, it was denoted as the background; otherwise, it was marked as the target. When the variance *G* of the two classes, according to Equation (1), was the maximum, the difference between the two classes was the largest, and the threshold *T* was best.

$$G = \omega_0 \times (u_0 - u)^2 + \omega_1 \times (u_1 - u)^2 \tag{1}$$

where ω_0 and u_0 are the proportion and average grey value of the background pixels, respectively; ω_1 and u_1 are the proportion and average grey value of the target pixels, respectively; and u is the total average gray level of the image. The above parameters can be calculated by Equation (2).

$$\begin{cases} \omega_0 = \sum_{0 \le k \le T} p(k) \\ \omega_1 = \sum_{T \le k \le m-1} p(k) \\ u_0 = \sum_{0 \le k \le T} \frac{kp(k)}{\omega_0} \\ u_1 = \sum_{T \le k \le m-1} \frac{kp(k)}{\omega_1} \\ u = \omega_0 \times u_0 + \omega_1 \times u_1 \end{cases} \tag{2}$$

where $p(k)$ is the probability with the gray value k, and m is the gray level.

The Otsu threshold method intelligently finds the appropriate threshold through the differences within the neighborhood of the seed region. This compensates for the disadvantage of a single threshold affecting the extraction effect, and it makes the segmentation process adaptive.

(3) **Region intelligence growth.** In Figure 6a,b, there are pixel numbers and pixel values of one image, respectively. Point 1 is the seed of regional growth, and 2, 3, 4, and 5 are the four neighborhood points of point 1. The absolute difference values of point 1 with its neighbor were calculated. If the value was less than the threshold *T*, the pixel's position would be the region's growth direction. In Figure 6, it can be seen that the area grew from point 1 to point 4 and then to point 6 until no more pixels met the condition. Thus, the region comprised points 1, 4, and 6. The final result is shown in Figure 6c.
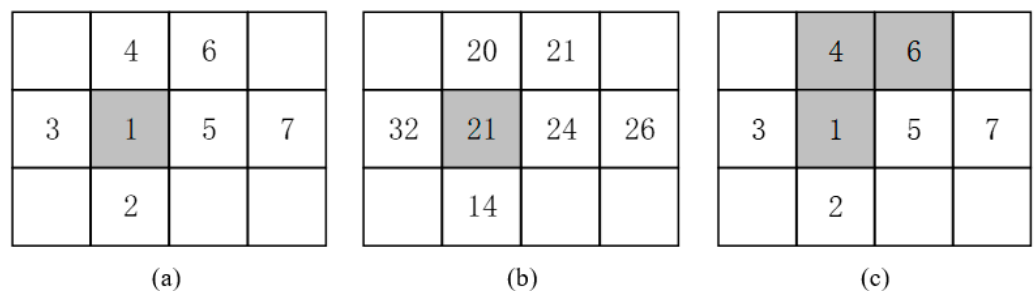
Figure 6. Principle of the region-growing method. (**a**) Pixel number, (**b**) Pixel value, (**c**) Growth direction.

With the seed point in the ocean as the starting point, the region gradually grew and merged until no pixel points were detected as increasing, and the region's growth ended. All pixels detected in the image were classified as the ocean, while the remaining were classified as land. Therefore, the image only had two categories: ocean and land.

(4) **Automatic edge detection.** The miniature objects, such as ships, islands, etc., were deleted to reduce the influence on the segmentation image. Then, Canny edge detection algorithms and morphological operators were used to automatically extract the boundary of the ocean and land, which represents the instantaneous waterline, as shown in Figure 7a.

For comparison, various algorithms were used in this study to automatically detect the edge in the image, as shown in Figure 7. The line segments inside the figure are boundary lines of the land features, the right and top boundary lines are instantaneous waterlines, and the left and bottom lines are imagery boundary lines. In Figure 7b–e, the image was cluttered by a large number of line segments, with voids and burrs causing the boundary line to be unsmooth and discontinuous. In Figure 7f, the amount of lines decreased significantly, and there were unclear and discontinuous boundary lines. In Figure 7a, the classification boundary of the land features was removed, and the detected instantaneous water boundary was continuous and smooth, without holes and burrs. Thus, the proposed method for instantaneous waterlines was optimal from the perspective of visual interpretation, which lays a solid foundation for the subsequent classification of features and the extraction of accurate coastlines.
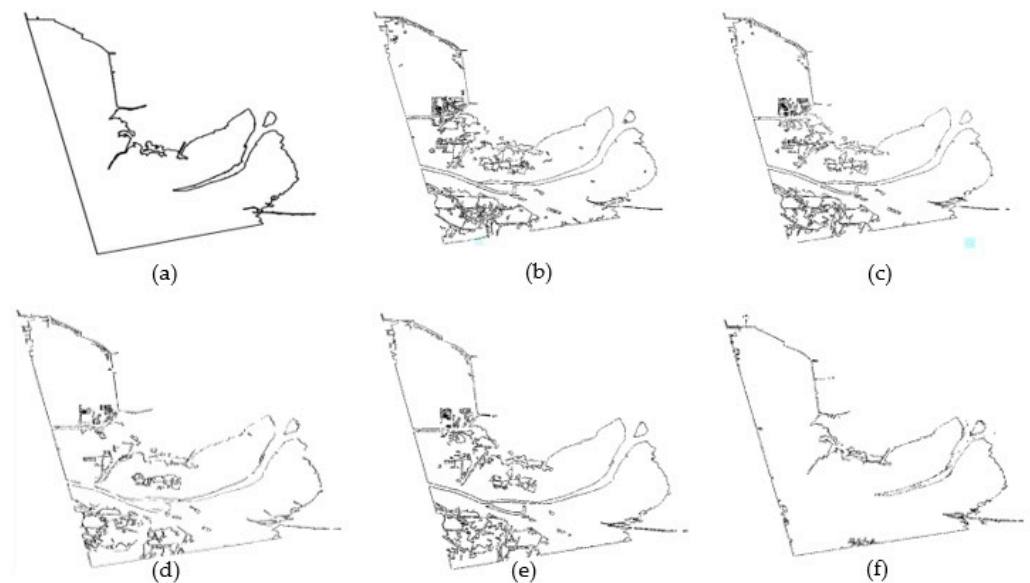
Figure 7. Instantaneous waterline extraction results. (**a**) Our method, (**b**) Canny edge detection method, (**c**) Otsu threshold algorithm, (**d**) Wavelet transform algorithm, (**e**) Tagged watershed algorithm, (**f**) Region growth algorithm.

The mask file was constructed with the instantaneous waterline, the ocean area was masked, and the land area was retained on the image, as shown in Figure 8. The above process reduced the amount of data and improved the processing speed of the image for the next stage.
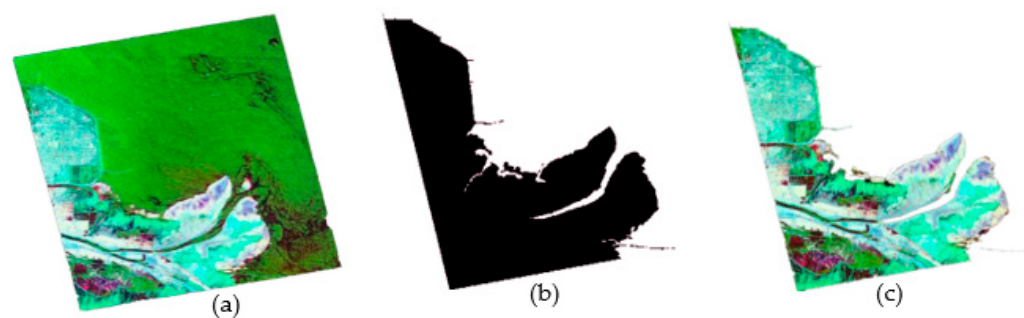
Figure 8. Image mask. (**a**) Feature image, (**b**) Mask file, (**c**) Land area.

2.2.4. Object-Oriented Automatic Segmentation and Classification

The conventional information extraction technology ignored the geometric structure of the entire patch nearby, which seriously restricted the extraction accuracy. Object-oriented

image analysis makes image automatic segmentation the target and takes full advantage of the shape, texture, context, spatial relationships, and other features.

Object-oriented technology was used to reclassify the land area on the image, which was inseparable from feature extraction and analysis. Therefore, 35 features were extracted from the SAR image, belonging to the original statistical features, polarization decomposition features, and texture features. Due to the high redundancy and poor salience of some features, the following were selected in this study: polarization statistical features, span, DoP, Huynen_T22, Cloude_T11, Freeman_Vol, and polarization scattering entropy in all 6 features with high significance and good separability. This allowed the following features to be distinguished: the tidal flat, willow forest, reed, suaeda salsa, aquaculture pond, spartina alterniflora, and water.

Based on the feature extraction and selection, a multi-scale segmentation method was used to segment the land features on the mask image. On the principle of the maximum average heterogeneity of pixels between objects and the maximum homogeneity of pixels within objects, the image was segmented by merging adjacent pixels and making full use of the adjacent spatial features, shape features, and polarization features. If the segmentation scale was small, the number of segmented objects would be enormous. Therefore, the fragmentation degree of objects after segmentation must be effectively controlled to avoid over-segmentation. After carrying out repeated experiments, approximately 1000 segmented objects were obtained when the segmentation scale was 160 and the shape factor was 0.5. At this time, the mean-variance of the segmented objects reached the maximum, the distinction between objects was the largest, and the segmentation effect was the best.

The segmented objects had no category label. To classify them, ten uniformly ground object samples of each category in the study area were selected, with a sample size of 15×15 pixels. With the multi-scale segmented objects as the basic unit and the preset samples and categories as constraints, the KNN classification algorithm was adopted to conduct the classification of 7 feature categories in the land area.

2.2.5. Instantaneous Waterline Correction Based on Classification

The instantaneous waterline was extracted from the dichotomous map of the land and ocean in Section 2.2.3. Therefore, image classification was the premise for instantaneous waterline extraction. However, correcting the instantaneous waterline to the coastline was also possible based on different feature categories.

As can be seen from Table 2, the features on both sides of the sandy coast, biological coast, and undeveloped silt coast were different. The tidal flat and sandy beaches were located on the seaward side of the coastline, while terrestrial vegetation and non-sandy features were located on the landward side. Therefore, the former was reclassified as a marine class, while the latter was a land class. If the water area on the classification map was near the instantaneous waterline, it was reclassified as the marine class; otherwise, it was reclassified as a land class. Then, the objects were merged, and only the two categories of the ocean and land were retained on the reclassification map.

After the reclassification of the land and ocean, the land area was reduced, and the reduced region was reclassified as the ocean, which reappeared compared with Figure 8c. The boundary line between the land and marine areas was redetected, which was regarded as the coastline. Compared with the instantaneous waterline, the coastline position was higher and offset toward the land. This process is represented in Figure 9. The above process corrected the instantaneous water boundaries at the sandy coast, biological coast, and undeveloped muddy coast to the coastline.
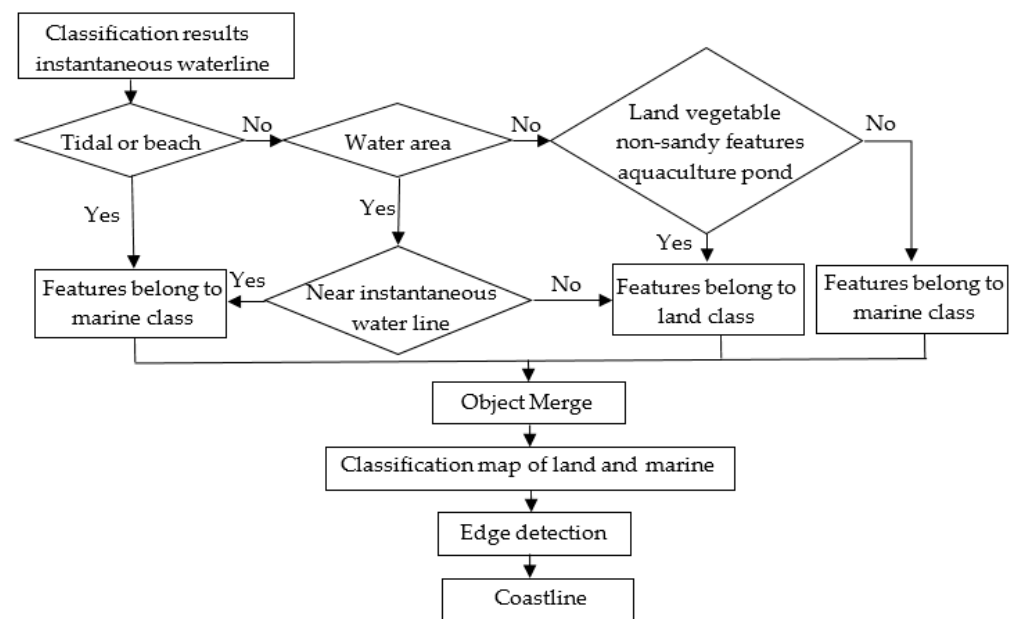
Figure 9. The flowchart of correction criteria based on the classification.

3. Results and Analysis

The result of segmentation and classification is presented in Figure 10. In Figure 10a, there are approximately 1000 segmented objects without a label. In Figure 10b, the features are classified as the tidal flat, willow forest, reed, suede salsa, spartina alterniflora, water, and aquaculture pond. Except for the aquaculture pond, the other six features are found near the coast.
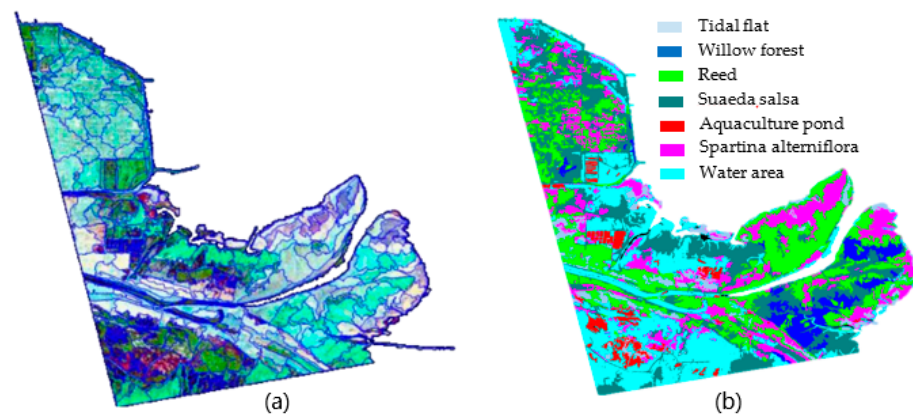

Figure 10. (**a**) Segmentation result of land area, (**b**) Classification result of land area.

To objectively evaluate the classification accuracy, the producer's accuracy (PA), the user's accuracy (UA), overall accuracy (OA), and Kappa coefficient were calculated, as shown in Table 3. The larger the four values, the better the classification result of the image. Table 3 shows that the OA was 92.56%, the Kappa coefficient was 0.91, and the PA and UA of the seven species reached above 91% and 87%. This indicates that there were few misclassifications and omissions, so the classification results were reliable.

The instantaneous waterline was corrected on the reclassified image. If the coastal feature was a tidal flat, the object was reclassified as being in the marine category, that is, the marine area grew. If the coastal feature was salt-tolerant plants, such as reed, willow forest, suaeda salsa, spartina alterniflora, etc., these features were combined and uniformly reclassified into the land category. After the above process, the SAR image was reclassified

into two categories of the ocean and land; then, the edge was detected as the final coastline, as shown in Figure 11.

Table 3. The accuracy of the classification.

Feature / Accuracy	Tidal Flat	Reed	Willow Forest	Spartina Alterniflora	Suaeda Salsa	Aquaculture Pond	Water
Producer's accuracy	92.65%	91.16%	95.82%	91.93%	91.55%	91.47%	93.46%
User's accuracy	92.76%	87.56%	92.95%	93.55%	95.94%	92.64%	92.96%
Overall accuracy				92.56%			
Kappa coefficient				0.91			
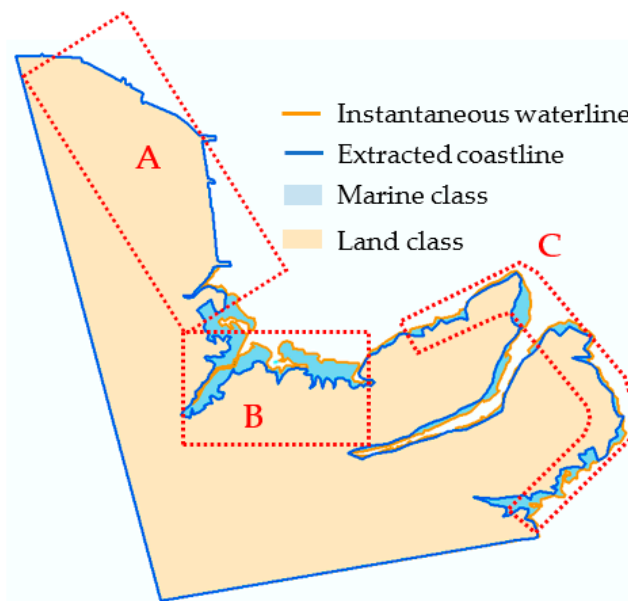
Figure 11. The result of instantaneous waterline correction. (Segment-A, Segment-B and Segment-C).

As can be seen in Figure 11, the instantaneous waterline coincided with the coastline in the A area where the artificial coast was located. However, the instantaneous waterline deviated from the shoreline in regions B and C where the undeveloped silty muddy coast and biological coast are situated. Therefore, regions B and C were local correction areas. After the object-oriented classification of the land area, the tidal flat and water area were classified as marine according to the criteria, and the other land objects were merged into the land. The water–land boundary was re-detected in the local areas, and the instantaneous correction from the instantaneous waterline to the coastline was achieved.

The manual visual interpretation method of the coastline using high-resolution optical images combined with interpretation characteristics was mature, and the accuracy was reliable after tidal correction [5,31]. The study selected a 2-m resolution of a GF-1 optical image on 21 September 2015, to detect the instantaneous waterline through visual interpretation, which was corrected to the coastline by the tide data. The coastline was verified by the field-measurement data. Although the acquisition time of the optical image was not entirely consistent with that of the SAR image, the coastline extracted from the GF-1 optical image can be used as verification data because the location of the coastline stays the same within a few days. Thus, the coastlines extracted by the two methods were superimposed, and no difference could be seen in the global graph. Therefore, the locally enlarged diagrams of the three coastlines were selected and they are shown in Figure 12.

(a)   (b)   (c)

——— Accurate coastline   ——— Extracted coastline
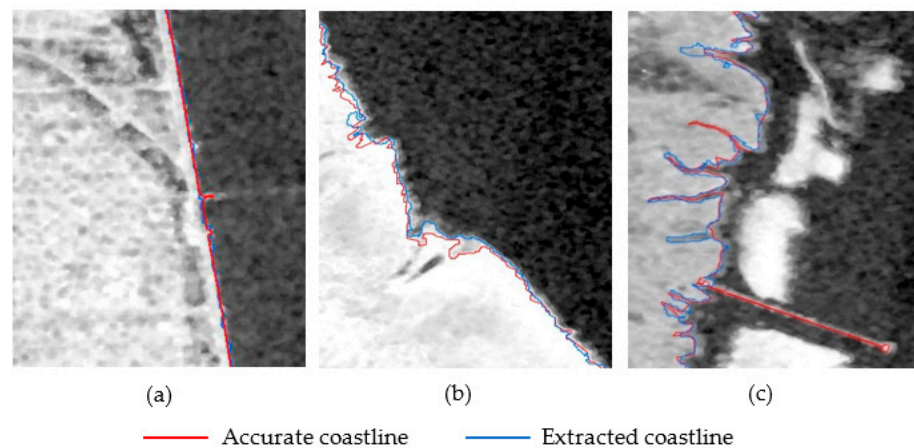
Figure 12. Superposition of real and extracted coastlines; (**a–c**) represents the artificial coastline, biological coastline, and undeveloped silty muddy coastline.

In Figure 12, the blue line overlaps with the red line in (a), and a global and local deviation exists between the two lines in (b) and (c). Equation (3) and Figure 13 were adapted to quantitatively evaluate the average deviation degree. The deviation degrees of the three types of coastlines in the Yellow River Delta were calculated, as shown in Table 4.

$$LM = \frac{S_A + S_B + S_C + S_D}{L_r} = \frac{S_\Delta}{L_r} \tag{3}$$

Table 4. Deviation degree of different coastline types.

Coastline Type	S_Δ/m^2	L_r/m	LM/m
Artificial Coastline	37,641	4626	8.1
Undeveloped Silty Muddy Coastlines	315,216	17,178	18.4
Biological Coastline	300,068	9936	30.2
Total	652,927	31,740	20.6
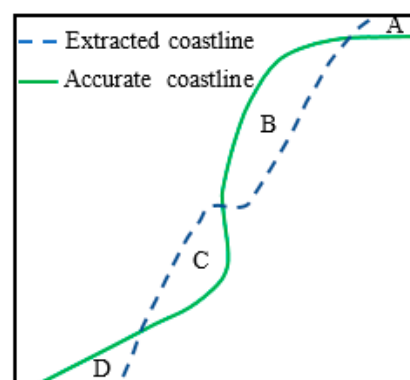
Figure 13. Two-line deviation diagram. A, B, C and D are areas where two coastlines intersect.

LM is the average deviation degree, and the unit is the meter; L_r is the length of the accurate coastline; S_A, S_B, S_C, S_D is the area of the intersection region; S_Δ is the total area.

Table 4 shows that the length of the artificial, undeveloped silty muddy, biological coastline was found to be 4.6 km, 17.1 km, and 9.9 km, respectively, and the deviation degree was 8.1 m, 18.4 m, and 30.2 m in the verification area. After geocoding, the resolution of the SAR image in this study was 11 m. The above deviation degree was less than the field distance represented by three pixels.

From the quantitative index, the deviation degree of the artificial shoreline was the smallest. The artificial coast was composed of permanent structures with regular shapes and precise positions, and the coastline was easy to accurately extract. The automatically extracted instantaneous waterline did not need to be corrected and coincided with the coastline.

The deviation index of the undeveloped silty coastline was moderate. There were large areas of tidal flats and various sizes of tidal trenches in the undeveloped silty coast. The tidal flat has prominent characteristics and differs significantly from seawater, so it was classified efficiently and accurately as a marine class in the reclassified image. The edge of the marine area and the land was automatically detected again. Due to the limitation of image resolution and the influence of the tide, the clarity of tidal trenches was different in various images. It was difficult to correct the instantaneous waterline to the coastline accurately.

The deviation index of the biological coastline was the largest. There were mainly reeds on the biological coast. Due to the influence of natural conditions and the growing season, the reeds were sparse, and the reeds appeared fuzzy in a 11 m-resolution SAR image. Thus, the boundary of the reeds was not apparent, but it coincided with the coastline, so the coastline was hard to determine precisely.

4. Conclusions and Future Work

The Radarsat-2 remote sensing image with high-resolution polarimetry was used in the study. Considering the definition of the coastline and the interpretation characteristics of different coast types, the instantaneous waterline can be divided into two types according to its position between coastlines. The first type is represented by the instantaneous waterline coinciding with the coastline in the artificial coast, rocky coast, and developed silty coast. The second type involves the instantaneous waterline deviating from the coastline in the sandy coast, biological coast, and undeveloped silty coast.

Based on the secondary division of the land and ocean, the secondary extraction boundary of the land and ocean, the classification of coastal features, and the correction criteria, the accurate coastline was extracted in this study. After the first division, the detected boundary of the land and ocean was the instantaneous waterline. A mask file was constructed by the instantaneous waterline to mask the ocean area and keep the land area only. Based on the feature extraction and screening of the SAR images, the image with only the land areas was divided into seven categories. The correction criterion was put forward according to the interpretation characteristics of different coast types and the classification of the surface features. Then, seven surface features were reclassified into the two categories of the land and ocean, realizing the secondary division. The boundary line was reextracted to obtain the coastline, and the correction of the local instantaneous waterline to the coastline was achieved. Detailed steps are as follows:

Firstly, the classification of the land and ocean was conducted. An intelligent and improved instantaneous waterline extraction algorithm was proposed by integrating the Otsu threshold method, the region-growing algorithm, Canny edge detection, and the morphology operator. The seed point was selected in the ocean as the starting point of regional growth, and an appropriate threshold was found adaptively. The pixel differences between the seed and neighbors were calculated; then, the growth direction of the ocean region was determined. Hence, the determination of the growth of the ocean was completed, and the image was divided into the two categories of the ocean and land. The edge tracking method was adapted to detect the boundary of the ocean and land, obtaining smooth and continuous instantaneous waterlines. Secondly, the object-oriented automatic classification of coastal features was carried out. Feature extraction and selection on the land image were carried out, and 35 dimensional features were extracted from the SAR image. Six features with high saliency and good separability were screened out. The optimal parameters of multi-scale segmentation were determined after repeated testing to complete the image segmentation. According to the selected sample points, the KNN classification algorithm was used to complete the image classification to obtain seven categories; the

overall accuracy reached 92%, and the Kappa coefficient was 0.91. Thirdly, the second division of the land–ocean boundary and the local correction of the instantaneous water boundary was carried out. The interpretation characteristics of different coastline types in satellite images were analyzed in detail, and the calibration criteria were proposed. According to the criterion, some land features, such as tidal flats, were reclassified as the ocean, which means that the marine area increased and the land area shrunk, so the second division between land and ocean was completed. The boundary between the land and ocean was redetected, the local correction of the extracted instantaneous water boundary was completed, and the accurate coastline was acquired. Finally, the coastline extracted in this study was verified with that extracted by a high- resolution optical satellite. After verification, the total length of the extracted shoreline in the area was 31.7 km, the overall deviation degree was 20.6 m, and the accuracy of the artificial shoreline was the highest, followed by the silt shoreline and the biological shoreline.

Only Radarsat-2 data were used in this study, and only three types of coastlines were found in the area. Therefore, the data source was singular, and there were multiple coastline types. Additional data sources and regions should be selected for further research, involving more coastal types. In addition, the correction criterion was carried out on the premise of a known coastline type. Therefore, further research focusing on establishing a method to automatically identify the coastline type and intelligently correct the instantaneous waterline from remote sensing images is required.

Author Contributions: Conceptualization, H.Z. and X.L.; Methodology, M.Y., M.X. and S.L.; Software, S.L. and J.W.; Formal analysis, H.Z. and X.L.; Resources, J.W., M.Y. and M.X.; Writing—original draft preparation, H.Z., X.L. and M.Y.; Writing—review and editing, S.L. and M.X. All authors have read and agreed to the published version of the manuscript.

Conflicts of Interest: The authors declare no conflict of interest.

References

1. Boak, E.H.; Turner, I.L. Shoreline definition and detection: A review. *J. Coast. Res.* **2005**, *21*, 688–703. [CrossRef]
2. Yasir, M.; Sheng, H.; Zheng, H.X.; Hossain, M.S. A spatiotemporal change detection analysis of coastline data in qingdao, east china. *Sci. Program.* **2021**, *2021*, 6632450. [CrossRef]
3. Sheng, H.; Guo, M.L.; Gan, Y.; Xu, M.; Liu, S.; Muhammad, Y.; Cui, J.; Wan, J. Coastline extraction based on multiscale segmentation and multi-level inheritance classification. *Front. Mar. Sci.* **2022**, *9*, 1031417.
4. Giang, T.L.; Bui, Q.T.; Nguyen, T.D.L.; Truong, Q.H.; Phan, T.T.; Nguyen, H.; Yasir, M.; Dang, K.B. Coastal landscape classification using convolutional neural network and remote sensing data in Vietnam. *J. Environ. Manag.* **2023**, *335*, 117537. [CrossRef]
5. Chen, C.; Liang, J.; Xie, F.; Hu, Z.; Sun, W.; Yang, G.; Yu, J.; Chen, L.; Wang, L.; Wang, L. Temporal and spatial variation of coastline using remote sensing images for Zhoushan archipelago, China. *Int. J. Appl. Earth Obs. Geoinf.* **2022**, *107*, 102711. [CrossRef]
6. Chen, C.; Fu, J.; Zhang, S.; Zhao, X. Coastline information extraction based on the tasseled cap transformation of Landsat-8 OLI images. *Estuar. Coast. Shelf Sci.* **2019**, *217*, 281–291. [CrossRef]
7. Hossain, M.S.; Yasir, M.; Wang, P.; Ullah, S.; Jahan, M.; Hui, S.; Zhao, Z. Automatic shoreline extraction and change detection: A study on the southeast coast of Bangladesh. *Mar. Geol.* **2021**, *441*, 106628. [CrossRef]
8. Yasir, M.; Sheng, H.; Fan, H.; Nazir, S.; Niang, A.J.; Salauddin, M.; Khan, S. Automatic coastline extraction and changes analysis using remote sensing and GIS technology. *IEEE Access* **2020**, *8*, 180156–180170. [CrossRef]
9. Liu, Y.; Wang, X.; Ling, F.; Xu, S.; Wang, C. Analysis of coastline extraction from Landsat-8 OLI imagery. *Water* **2017**, *9*, 816. [CrossRef]
10. Ju, C.; Jing, L.H.; Li, H.; Xu, W.; Dong, Y. The coastline automatic extraction research of object-oriented based on the GF-1 remote sensing image: A case in Qinhuangdao. *Geomat. Spat. Inf. Technol.* **2017**, *40*, 30–38.
11. Yang, Z.; Yu, X.; Dedman, S.; Rosso, M.; Zhu, J.; Yang, J.; Xia, Y.; Tian, Y.; Zhang, G.; Wang, J. UAV remote sensing applications in marine monitoring: Knowledge visualization and review. *Sci. Total Environ.* **2022**, *838*, 155939. [CrossRef] [PubMed]

12. Yue, Z.; Zhou, W.; Li, T. Impact of the Indian Ocean dipole on evolution of the subsequent ENSO: Relative roles of dynamic and thermodynamic processes. *J. Clim.* **2021**, *34*, 3591–3607. [CrossRef]

13. Yang, M.; Wang, H.; Hu, K.; Yin, G.; Wei, Z. IA-Net: An Inception–Attention-Module-Based Network for Classifying Underwater Images from Others. *IEEE J. Ocean. Eng.* **2022**, *47*, 704–717. [CrossRef]

14. Wang, X.; Lyu, X. Experimental study on vertical water entry of twin spheres side-by-side. *Ocean. Eng.* **2021**, *221*, 108508. [CrossRef]

15. Zhou, G.; Li, C.; Zhang, D.; Liu, D.; Zhou, X.; Zhan, J. Overview of underwater transmission characteristics of oceanic LiDAR. *IEEE J. Sel. Top. Appl. Earth Obs. Remote Sens.* **2021**, *14*, 8144–8159. [CrossRef]

16. Yuan, L.; Yang, D.; Wu, X.; He, W.; Kong, Y.; Ramsey, T.S.; Degefu, D.M. Development of multidimensional water poverty in the Yangtze River Economic Belt, China. *J. Environ. Manag.* **2023**, *325*, 116608. [CrossRef]

17. Liu, Z.; Xu, J.; Liu, M.; Yin, Z.; Liu, X.; Yin, L.; Zheng, W. Remote sensing and geostatistics in urban water-resource monitoring: A review. *Mar. Freshw. Res.* **2023**. [CrossRef]

18. Zhu, X.; Xu, Z.; Liu, Z.; Liu, M.; Yin, Z.; Yin, L.; Zheng, W. Impact of dam construction on precipitation: A regional perspective. *Mar. Freshw. Res.* **2022**. [CrossRef]

19. Tian, Y.; Yang, Z.; Yu, X.; Jia, Z.; Rosso, M.; Dedman, S.; Zhu, J.; Xia, Y.; Zhang, G.; Yang, J. Can we quantify the aquatic environmental plastic load from aquaculture? *Water Res.* **2022**, *219*, 118551. [CrossRef]

20. Ferrentino, E.; Buono, A.; Nunziata, F.; Marino, A.; Migliaccio, M. On the Use of Multipolarization Satellite SAR Data for Coastline Extraction in Harsh Coastal Environments: The Case of Solway Firth. *IEEE J. Sel. Top. Appl. Earth Obs. Remote Sens.* **2021**, *14*, 249–257. [CrossRef]

21. Incekara, A.H.; Seker, D.Z.; Bayram, B. Qualifying the LIDAR-derived intensity image as an infrared band in NDWI-based shoreline extraction. *IEEE J. Sel. Top. Appl. Earth Obs. Remote Sens.* **2018**, *11*, 5053–5062. [CrossRef]

22. Li, L.; Ma, L.; Jiao, L.; Liu, F.; Sun, Q.; Zhao, J. Complex contourlet-CNN for polarimetric SAR image classification. *Pattern Recognit.* **2020**, *100*, 107110. [CrossRef]

23. She, X.; Lei, B. New polarimetric entropy based coastline extraction method for PolSAR images. *Foreign Electron. Meas. Technol.* **2017**, *36*, 76–82.

24. Paes, R.L.; Nunziata, F.; Migliaccio, M. Coastline extraction and coastal area classification via SAR hybrid-polarimetry architecture. In Proceedings of the 2015 IEEE International Geoscience and Remote Sensing Symposium (IGARSS), Milan, Italy, 26–31 July 2015; pp. 3798–3801.

25. Nunziata, F.; Buono, A.; Migliaccio, M.; Benassai, G. Dual-polarimetric C-and X-band SAR data for coastline extraction. *IEEE J. Sel. Top. Appl. Earth Obs. Remote Sens.* **2016**, *9*, 4921–4928. [CrossRef]

26. Ferrentino, E.; Nunziata, F.; Migliaccio, M. Full-polarimetric SAR measurements for coastline extraction and coastal area classification. *Int. J. Remote Sens.* **2017**, *38*, 7405–7421. [CrossRef]

27. Modava, M.; Akbarizadeh, G.; Soroosh, M. Integration of spectral histogram and level set for coastline detection in SAR images. *IEEE Trans. Aerosp. Electron. Syst.* **2018**, *55*, 810–819. [CrossRef]

28. Liu, D.; Han, L. Coastline Extraction from GF-3 SAR Images Using LKDACM and GMM Algorithms. *Int. J. Pattern Recognit. Artif. Intell.* **2022**, *36*, 2254001. [CrossRef]

29. Xukai, Z.; Xia, Z.; Banghui, Y.; Zhi, Z.; Kun, S. Coast-line extraction using remote sensing based on coastal type and tidal correction. *Remote Sens. Land Resour.* **2013**, *25*, 91–97.

30. Liu, X.; Gao, Z.; Ning, J.; Yu, X.; Zhang, Y. An improved method for mapping tidal flats based on remote sensing waterlines: A case study in the Bohai Rim, China. *IEEE J. Sel. Top. Appl. Earth Obs. Remote Sens.* **2016**, *9*, 5123–5129. [CrossRef]

31. Wu, Y.Q.; Liu, Z.L. Research progress on methods of automatic coastline extraction based on remote sensing images. *J. Remote Sens* **2019**, *23*, 582–602.

32. Moore, L.J. Shoreline mapping techniques. *J. Coast. Res.* **2000**, *16*, 111–124.

33. Sun, W.; Ma, Y.; Zhang, J.; Liu, S.; Ren, G. Study of remote sensing interpretation keys and extraction technique of different types of shoreline. *Bull. Surv. Mapp.* **2011**, *3*, 41–44.

34. Guo, Z.; Yonghua, J.; Litao, L.; Mingjun, D.; Ruishan, Z. Research progress of high-resolution optical/SAR satellite geometric radiometric calibration. *Acta Geod. Cartogr. Sin* **2019**, *48*, 1604–1623.

35. Wei, X.; Zhang, L.; He, X.; Liao, M. Spaceborne SAR image geocoding with RFM model. *J. Remote Sens.* **2012**, *16*, 1089–1099.

36. Vitale, S.; Cozzolino, D.; Scarpa, G.; Verdoliva, L.; Poggi, G. Guided patchwise nonlocal SAR despeckling. *IEEE Trans. Geosci. Remote Sens.* **2019**, *57*, 6484–6498. [CrossRef]

37. Pan, T.; Peng, D.; Yang, W.; Li, H. A filter for SAR image despeckling using pre-trained convolutional neural network model. *Remote Sens.* **2019**, *11*, 2379. [CrossRef]

38. Chen, X.; Sun, J.; Yin, K.; Yu, J. Sea-land segmentation algorithm of SAR image based on Otsu method and statistical characteristic of sea area. *J. Date Acquis. Process* **2014**, *29*, 603–608.

39. Wang, D.L.; Yang, Y. Coastline extraction with optimal threshold from SAR images using kernel estimation. *Radar Sci. Technol.* **2019**, *17*, 310–318.

40. Zhan, Y.; Zhu, L.; Sun, Y.; Su, X.; Hou, H. Automatic extraction of coastline via spectral angle-distance similarity growth model. *J. Remote Sens.* **2017**, *21*, 458–469.

41. Zhang, T.; Yang, X.; Hu, S.; Su, F. Extraction of coastline in aquaculture coast from multispectral remote sensing images: Object-based region growing integrating edge detection. *Remote Sens.* **2013**, *5*, 4470–4487. [CrossRef]

42. Modava, M.; Akbarizadeh, G. Coastline extraction from SAR images using spatial fuzzy clustering and the active contour method. *Int. J. Remote Sens.* **2017**, *38*, 355–370. [CrossRef]